Inorganics **2015**, *3*, 194-218; doi:10.3390/inorganics3020194

OPEN ACCESS

inorganics

ISSN 2304-6740

www.mdpi.com/journal/inorganics

Article

Single-Crystal to Single-Crystal Reversible Transformations Induced by Thermal Dehydration in Keggin-Type Polyoxometalates Decorated with Copper(II)-Picolinate Complexes: The Structure Directing Role of Guanidinium

Aroa Pache [1], Santiago Reinoso [1], Leire San Felices [2], Amaia Iturrospe [1], Luis Lezama [1,3,*] and Juan M. Gutiérrez-Zorrilla [1,3,*]

[1] Departamento de Química Inorgánica, Facultad de Ciencia y Tecnología, Universidad del País Vasco UPV/EHU, P. O. Box 644, Bilbao 48080, Spain; E-Mails: aroa.pache@ehu.es (A.P.); santiago.reinoso@ehu.es (S.R.); amaia.iturrospe@ehu.es (A.I.)

[2] Servicios Generales de Investigación SGIker, Universidad del País Vasco UPV/EHU, P. O. Box 644, Bilbao 48080, Spain; E-Mail: leire.sanfelices@ehu.es

[3] BCMaterials, Parque Científico y Tecnológico de Bizkaia, Edificio 500, Derio 48160, Spain

* Authors to whom correspondence should be addressed; E-Mails: luis.lezama@ehu.es (L.L.); juanma.zorrilla@ehu.es (J.M.G.-Z.); Tel.: +34-94-601-2703 (L.L.); +34-94-601-5522 (J.M.G.-Z.); Fax: +34-94-601-3500 (L.L. & J.M.G.-Z.).

Academic Editors: Greta Ricarda Patzke and Pierre-Emmanuel Car

Received: 13 April 2015 / Accepted: 19 May 2015 / Published: 27 May 2015

Abstract: Three new hybrid inorganic-metalorganic compounds containing Keggin-type polyoxometalates, neutral copper(II)-picolinate complexes and guanidinium cations have been synthesized in bench conditions and characterized by elemental analysis, infrared spectroscopy and single-crystal X-ray diffraction: the isostructural $[C(NH_2)_3]_4[\{XW_{12}O_{40}\}\{Cu_2(pic)_4\}]\cdot[Cu_2(pic)_4(H_2O)]_2\cdot 6H_2O$ [X = Si (**1**), Ge (**3**)] and $[C(NH_2)_3]_8[\{SiW_{12}O_{40}\}_2\{Cu(pic)_2\}_3\{Cu_2(pic)_4(H_2O)\}_2]\cdot 8H_2O$ (**2**). The three compounds show a pronounced two-dimensional character owing to the structure-directing role of guanidinium. In **1** and **3**, layers of $[\{XW_{12}O_{40}\}\{Cu_2(pic)_4\}]_n^{4n-}$ hybrid POM chains and layers of $[Cu_2(pic)_4(H_2O)]$ complexes and $[C(NH_2)_3]^+$ cations pack alternately along the *z* axis. The hydrogen-bonding network established by guanidinium leads to a trihexagonal tiling arrangement of all copper(II)-picolinate species. In contrast, layers of $[C(NH_2)_3]^+$-linked $[\{SiW_{12}O_{40}\}_2\{Cu(pic)_2\}_3]_n^{8n-}$ double chains where each Keggin cluster displays a $\{Cu_2(pic)_4(H_2O)\}$ moiety pointing at the intralamellar space are observed in **2**.

The thermal stability of **1**–**3** has been studied by thermogravimetric analyses and variable temperature powder X-ray diffraction. Compounds **1** and **3** undergo single-crystal to single-crystal transformations promoted by reversible dehydration processes and the structures of the corresponding anhydrous phases **1a** and **3a** have been established. Despite the fact that the $[Cu_2(pic)_4(H_2O)]$ dimeric complexes split into $[Cu(pic)_2]$ monomers upon dehydration, the packing remains almost unaltered thanks to the preservation of the hydrogen-bonding network established by guanidinium and its associated Kagome-type lattice. Splitting of the dimeric complexes has been correlated with the electron paramagnetic resonance spectra.

Keywords: polyoxometalates; crystal-to-crystal transformations; guanidinium

1. Introduction

Over the past several years, the large family of anionic metal-oxygen clusters known as polyoxometalates (POMs) has been thoroughly employed as building blocks to construct a variety of inorganic-organic hybrid compounds [1–7]. The assembly of POMs with transition metal complexes bearing organic ligands (TMCs) is an effective strategy for designing such type of compounds. The POMs may adopt a variety of roles in these types of hybrid systems: (1) charge compensating anions; (2) ligands directly bonded to TMCs; (3) templates inducing the self-assembly of MOFs [8–13]. The clusters can act as peculiar inorganic ligands able to bind several TMCs through terminal or bridging oxygen atoms [14–16], and this often results in assemblies with extended structures. Thus, many high-dimensional POM-based hybrids have been successfully synthesized to date [17–19].

A critical factor for the construction of such architectures rests on the choice of appropriate organic ligands. For example, carboxylate derivatives of heterocyclic amines with mixed *N*,*O*-donor atoms are likely to afford polymeric structures with high dimensionalities among the vast library of polydentate ligands [20–22]. One way of better controlling the structure of the hybrid compound is the use directing agents able to form extensive networks of weak intermolecular interactions. A great deal of attention has been paid to the structure-directing role of several organic species and a surprising variety of organically-templated inorganic frameworks are found in the literature [23–25]. Guanidinium has shown up as an excellent template because it can establish massive hydrogen-bonding networks due to its high molecular symmetry and extremely weak acid character [26]. This cation has been successfully applied in POM chemistry not only as a template of high-dimensional frameworks but also as a selective crystallizing agent for minor POM species in mixed solutions [27–29].

We have recently reported a series of hybrid compounds based on $[XW_{12}O_{40}]^{4-}$ Keggin-type anions (X = Si, Ge) and copper(II) complexes of tetradentate bis(aminopyridil) ligands that can reversibly undergo thermal desorption of water via single-crystal to single-crystal (SCSC) transformations with significant modifications in the bonding and coordination geometry around the Cu^{II} centers [30,31]. To date, full studies on SCSC transformations are still scarce for POM-based compounds [32–38] and those involving the temperature as the external stimulus inducing the solid-state phase transition are limited to the low-temperature polymorphs of $[Tm_2(H_2O)_{14}(H_6CrMo_6O_{24})][H_6CrMo_6O_{24}]\cdot 16H_2O$ and

$[C(NH_2)_3]_6[Mo_7O_{24}]\cdot H_2O$, to the monitoring of the dehydration in the $H_5PV_2Mo_{10}O_{40}\cdot 36H_2O$ acid and in the porous $[Co_2(ppca)_2(H_2O)(V_4O_{12})_{0.5}]$ (ppca = 4-(pyridin-4-yl)pyridine-2-carboxylic acid) hybrid material [39–42]. This scarcity is certainly remarkable because the study of solid-state phase transitions induced by external stimuli such as the temperature, redox processes, or the interaction with guest molecules is at the forefront of the crystal engineering [43]. For example, several reports on SCSC transformations triggered by the removal, incorporation and/or exchange of solvent guest molecules can be found in the literature for related systems like metalorganic framework (MOF) materials [44–47]. These processes are often referred to as dynamic structural changes associated to compounds classified as third generation materials with potential applications in gas storage and separation, chemical sensing or magnetic switching [48,49].

We now intend to explore the thermostructural behavior of other hybrid systems related to our previous Keggin/bis(aminopyridyl) compounds to evaluate the role of the organic component in facilitating such SCSC transitions. We have first focused our studies on *N*,*O*-polydentate heterocyclic ligands, which represent a great first choice for the preparation of extended structures [50–52], and their concerted action with templating cations like $[C(NH_2)_3]^+$. Keggin-type anions have been kept as the inorganic building blocks in our systems because (i) these clusters and their numerous derivatives represent the most archetypal class of heteropolyoxometalates [53,54] and (ii) they are widely known to give rise to highly intricate hybrid structures by coordinating a large number of TMCs simultaneously [6,55].

In this work, we report the synthesis, crystal structure, thermal behavior and electron paramagnetic resonance (EPR) spectra of a series of guanidinium-templated compounds based on Keggin-typeanions and copper(II)-picolinate complexes: $[C(NH_2)_3]_4[\{XW_{12}O_{40}\}\{Cu_2(pic)_4\}]\cdot[Cu_2(pic)_4(H_2O)]_2\cdot 6H_2O$ [X = Si (**1**), Ge (**3**)] and $[C(NH_2)_3]_8[\{SiW_{12}O_{40}\}_2\{Cu(pic)_2\}_3\{Cu_2(pic)_4(H_2O)\}_2]\cdot 8H_2O$ (**2**). Compounds **1** and **3** undergo SCSC transformations promoted by thermally induced, reversible dehydration processes and the structures of the anhydrous phases $[C(NH_2)_3]_4[\{XW_{12}O_{40}\}\{Cu_2(pic)_4\}]\cdot[Cu(pic)_2]_4$ [X = Si (**1a**), Ge (**3a**)] have also been determined by single crystal X-ray diffraction.

2. Results and Discussion

2.1. Synthesis and Infrared Spectroscopy

Compounds **1**–**3** were prepared under mild bench conditions from the $[C(NH_2)_3]^+$-directed self-assembly of $[XW_{12}O_{40}]^{4-}$ (X = Si, Ge) and $[Cu(pic)_2]$ building blocks in acidic aqueous medium (pH 3–3.5) at room temperature. Both types of building blocks were generated in situ from $[XW_{11}O_{39}]^{8-}$ POM precursors, a copper(II) source and the pic ligand in its acidic form. For X = Si, different POM:Cu:pic ratios were tested and the solid products obtained upon evaporation were characterized preliminarily by IR spectroscopy. For a 1:3:2 ratio, a mixture of blue crystals of a copper(II)-picolinate complex and a white powder corresponding to a guanidinium salt of the plenary $[SiW_{12}O_{40}]^{4-}$ anion was obtained. Lowering the amount of Cu^{II} ions to a 1:2:2 ratio led to co-crystallization of the complex with compound **1** as the minor fraction. Crystallization of the former was avoided by using a 1:1:2 ratio. Formation of **1** was maximized in these conditions, but

crystallization of a small amount of a second crystalline phase (compound **2**) was in turn observed. Crystals of **1** are formed before those of **2** and this fact could be explained on the basis of the different POM:Cu ratio in both compounds: 1:6 and 2:7, respectively. The initial POM:Cu ratio in the reaction mixture is 1:1, and hence the compound with the highest Cu^{II} content (**1**) tends to crystallize first. The amount of the copper(II)-picolinate complex in solution decreases with respect to that of the POM when **1** crystallizes and this in turn favors the formation of a small amount of **2** with the highest POM content to re-equilibrate the POM:Cu ratio. All attempts of improving the synthetic procedure to avoid formation of mixtures were unsuccessful. While **1** is obtained as the major phase in a mixture of crystals with the side-product **2**, the isostructural **3** is isolated as a single crystalline phase when $[GeW_{11}O_{39}]^{8-}$ is used under the same synthetic conditions and no traces of a hypothetical Ge-containing analogue of **2** are observed by powder X-ray diffraction analysis (Figure S1). It is also worth noting that we never obtained any spectroscopic indication of a compound containing copper(II)-monosubstituted $[XW_{11}O_{39}Cu(H_2O)]^{6-}$ species in spite of using monolacunary Keggin-type anions as precursors. These species are known to be metastable in weakly acidic conditions (typically in the pH range 4–6 for heteropolyoxotungstates), and hence slow conversion into the plenary clusters seems reasonable after considering the pH values of our reaction mixtures. Since **1**–**3** contain plenary Keggin-type anions as the inorganic building block, we also performed a set of reactions using $[XW_{12}O_{40}]^{4-}$ POMs as the precursors. In all cases, powders containing these clusters and copper(II)-picolinate complexes were obtained according to IR spectroscopy. These powders could not be recrystallized or unequivocally identified as compounds **1**–**3** on the basis of powder X-ray diffraction. Thus, the kinetically slow $[XW_{11}O_{39}]^{8-}$ to $[XW_{12}O_{40}]^{84-}$ conversion appears to be a key factor in isolating our compounds as single crystals suitable for further structural characterization.

The infrared spectra of **1**–**3** (Figure S2) show the characteristic features of the $[\alpha\text{-}XW_{12}O_{40}]^{4-}$ Keggin-type anion in the region below 1000 cm^{-1} with bands of strong intensity corresponding to the antisymmetric stretching of the W–O_t and W–O_b–W bonds that appear at 970 and *ca.* 800 cm^{-1} for X = Si and 966 and 787 cm^{-1} for X = Ge, respectively. The grafting of the copper(II)-picolinate complexes onto the POM surfaces shift the above signals by 10 cm^{-1} compared to those of the clusters in the potassium salts and leads also to the appearance of additional peaks in the 760–660 cm^{-1} range related to the Cu–O and Cu–N stretching among other vibrations. The metalorganic region above 1000 cm^{-1} is dominated by signals of medium to strong intensity that are observed in the 1160–1684 cm^{-1} range and associate to C=C and C=N stretching vibrations in the pyridine rings.

*2.2. Crystal Structures of Compounds **1**–**3***

Compounds **1** and **3** are isostructural and crystallize in the triclinic space group *P*–1 with the following molecules in the asymmetric unit: one half of a centrosymmetric $\{XW_{12}O_{40}\}$ Keggin cluster (X = Si, Ge), one half of a centrosymmetric $\{Cu_2(pic)_4\}$ dinuclear complex supported on the cluster, two halfs of an isolated dimeric unit $[Cu_2(pic)_4(H_2O)]$, two $[C(NH_2)_3]^+$ cations and three H_2O molecules. Compound **2** also crystallizes in the space group *P*–1 and its asymmetric unit contains one $\{SiW_{12}O_{40}\}$ Keggin cluster, one supported $\{Cu_2(pic)_4(H_2O)\}$ dinuclear complex, one half of a centrosymmetric $\{Cu(pic)_2\}$ monomeric unit connected to the cluster, another $\{Cu(pic)_2\}$ complex also connected to the cluster, four $[C(NH_2)_3]^+$ cations and four H_2O molecules (Figure 1).

The inorganic $[XW_{12}O_{40}]^{4-}$ building block in all compounds shows the characteristic structure of the α-Keggin isomer consisting of a central XO_4 tetrahedron surrounded by four edge-shared W_3O_{13} trimers, all of them linked via corner-sharing in ideal T_d symmetry. In the case of **1** and **3**, the Keggin anion lies on a center of inversion with the tetrahedral XO_4 group disordered over two crystallographic positions, which leads to its observation as a XO_8 cube with half-occupied O sites (Figure 1, left). Table S1 displays ranges of W–O and X–O bond lengths compared to those of the DFT-optimized Keggin anion [56].

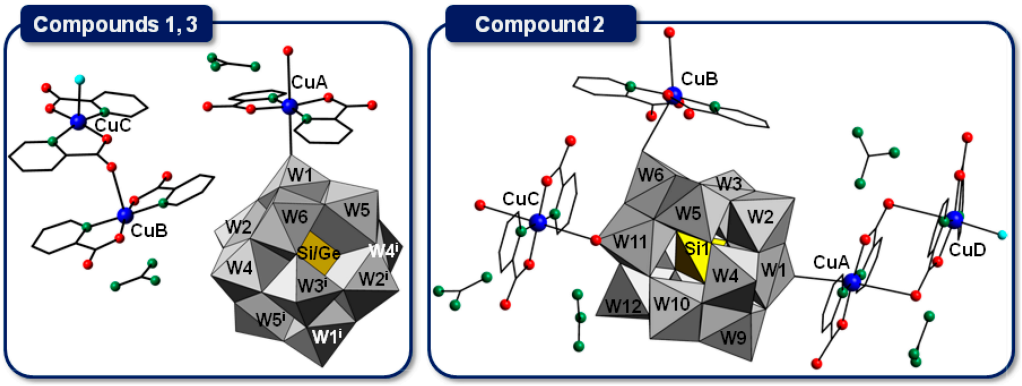

Figure 1. Connectivity between building blocks in the asymmetric units of **1**–**3**. Color code: W, gray polyhedra; Si/Ge, yellow polyhedra; Cu, blue spheres; N, green spheres; O, red spheres for O_{pic} or O_{POM} atoms and cyan spheres for terminal aqua ligands; C, black sticks. Symmetry code: (i) $-x, -y, -z$.

2.2.1. Copper(II)-Picolinate Complexes

The title compounds contain different types of neutral copper(II) complexes with the ligand 2-picolinate. In all of these complexes, the Cu^{II} atom shows axial-type coordination geometry with two *trans*-related organic ligands forming the basal or equatorial plane (Figure 2). Selected bond lengths compared to those found in the anhydrous phases **1a** and **3a** are listed in Table 1.

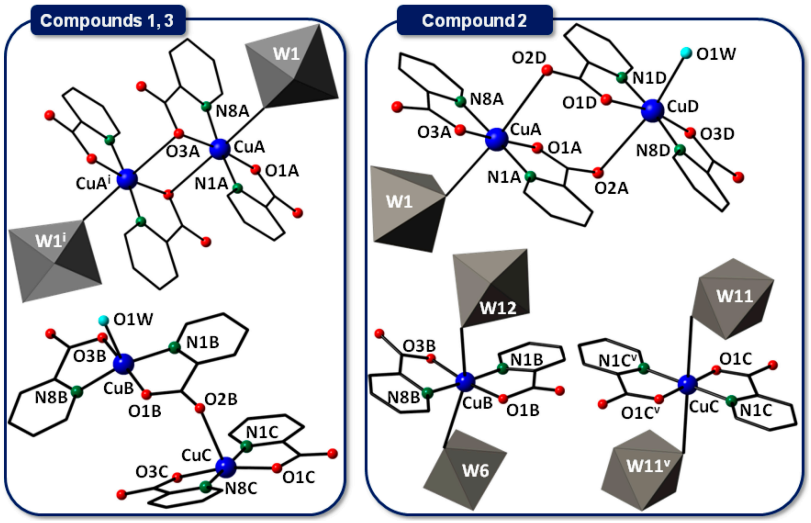

Figure 2. Copper(II)-picolinate complexes with atom labeling in **1**–**3** (for the symmetry codes i and v see Table 1).

Table 1. Bond lengths and intradimeric Cu···Cu distances (Å) for the copper(II)-picolinate complexes in **1**–**3** compared to those in the anhydrous phases **1a** and **3a**.

Bond	1	1a	3	3a	Bond	2
CuA–N1A	1.964(8)	1.959(9)	1.965(8)	1.956(16)	CuA–N1A	1.98(2)
CuA–O1A	1.956(7)	1.962(7)	1.958(7)	1.972(14)	CuA–O1A	1.91(2)
CuA–N8A	1.965(9)	1.953(8)	1.954(8)	1.961(16)	CuA–N8A	1.96(2)
CuA–O3A	1.973(7)	1.970(7)	1.963(7)	1.975(14)	CuA–O3A	1.97(2)
CuA–O1/	2.459(18)/	2.527(17)/	2.468(17)/	2.48(3)/	CuA–O1	2.57(2)
–O1Z	2.349(18)	2.352(15)	2.346(17)	2.36(2)	CuA–O2D^{iii}	2.93(2)
CuA–O3A^{i}	2.778(8)	2.807(7)	2.774(7)	2.846(14)		
CuB–N1B	1.978(9)	1.956(8)	1.977(9)	1.972(16)	CuB–N1B	1.95(2)
CuB–O1B	1.972(8)	1.939(7)	1.970(7)	1.940(15)	CuB–O1B	1.96(2)
CuB–N8B	1.981(9)	1.956(9)	1.975(9)	1.944(17)	CuB–N8B	1.98(3)
CuB–O3B	1.969(8)	1.951(7)	1.968(7)	1.943(15)	CuB–O3B	1.89(2)
CuB–O1W	2.253(9)	–	2.258(8)	–	CuB–O12/	2.77(2)
					–O12Z	2.98(5)
					CuB–O6^{iv}	2.77(2)
CuC–N1C	1.973(9)	1.964(9)	1.972(9)	1.985(18)	CuC–N1C	1.958(18)
CuC–O1C	1.949(9)	1.953(8)	1.951(8)	1.931(16)	CuC–O1C	1.888(16)
CuC–N8C	1.971(9)	1.962(9)	1.966(9)	1.96(2)	CuC–N1C^{v}	1.958(18)
CuC–O3C	1.951(8)	1.928(8)	1.946(8)	1.945(16)	CuC–O1C^{v}	1.888(16)
CuC–O2B^{ii}	2.488(8)	3.310(8)	2.490(8)	3.314(18)	CuC–O11	2.909(19)
					CuC–O11^{v}	2.909(19)
					CuD–N1D	1.96(3)
					CuD–O1D	1.97(2)
					CuD–N8D	1.97(2)
					CuD–O3D	1.96(2)
					CuD–O1W	2.29(3)
					CuD–O2A^{iii}	2.97(3)
CuA···CuA^{i}	3.572(2)	3.554(2)	3.568(2)	3.617(3)	CuA···CuD^{iii}	5.305(6)
CuB···CuC^{ii}	5.538(3)	5.458(2)	5.540(2)	5.498(5)		

Note: Symmetry Codes: (i) 1–*x*, 1–*y*, –*z*; (ii) –*x*, 1–*y*, –*z*; (iii) 2–*x*, –*y*, –*z*; (iv) *x*, 1+*y*, *z*; (v) 1–*x*, –*y*, 1–*z*.

Two different types of dinuclear complexes coexist in the structures of **1** and **3**. The metalorganic $\{Cu_2(pic)_4\}$ subunit is composed of two centrosymmetrically related $\{CuA(pic)_2\}$ fragments where the CuA atom is involved in a $CuN_2O_2O'_2$ chromophore with tetragonally elongated octahedral geometry. One of the axial positions in each CuA center is occupied by one of the O_{pic} atoms forming the equatorial CuN_2O_2 plane of the neighboring fragment, in such a way that a dimeric complex with *equatorial-axial* $Cu_2(\mu^2\text{-}O_{pic})_2$ rhomboid core is formed. A terminal O_{POM} atom (disordered over two sites, e.g., O1/O1Z in Table 1) occupies the second axial position, and hence the $\{Cu_2(pic)_4\}$ subunits link the Keggin clusters in hybrid $[\{XW_{12}O_{40}\}\{Cu_2(pic)_4\}]^{4-}$ chains with alternate inorganic and metalorganic building blocks. In contrast, the $[Cu_2(pic)_4(H_2O)]$ moiety is formed by one $\{CuC(pic)_2\}$ and one $\{CuB(pic)_2(H_2O)\}$ fragments where both Cu^{II} atoms show CuN_2O_2O' chromophores with distorted square-pyramidal geometry. A water molecule is located at the apical position of CuB, whereas that of CuC is occupied by one of the O_{pic} atoms that are not involved in the basal CuN_2O_2

plane of CuB. Therefore, the two Cu^{II} centers in this moiety are linked by a single pic bridging ligand acting in μ^2-κ^2N,O^1:κ^1O^2 coordination mode.

In the case of **2**, the structure contains one dinuclear and two crystallographically independent mononuclear complexes where the $CuN_2O_2O'_2$ coordination environment around all Cu^{II} centers is tetragonally elongated octahedral. In both monomeric subunits, the axial positions of the CuB and CuC atoms are occupied by terminal O_{POM} atoms. Thus, the {CuB(pic)$_2$} subunits link the Keggin clusters in a one-dimensional assembly of alternate inorganic and metalorganic building blocks, whereas the {CuC(pic)$_2$} subunits act as connectors between pairs of such hybrid chains to lead to the backbone of the $[\{SiW_{12}O_{40}\}_2\{Cu(pic)_2\}_3\{Cu_2(pic)_4(H_2O)\}_2]_n^{8n-}$ polymer. The dinuclear {Cu_2(pic)$_4$(H_2O)} subunit is made of one {CuA(pic)$_2$} and one {CuD(pic)$_2$(H_2O)} fragments linked in *equatorial-axial* fashion by two pic ligands in μ^2-κ^2N,O^1:κ^1O^2 bridging mode. Thus, each Cu^{II} center shows at axial positions one of the O_{pic} atoms that are not involved in the equatorial plane of the neighboring fragment. The coordination geometry of CuD is completed with one aqua ligand, whereas CuA axially anchors to a terminal O_{POM} atom, in such a way that the double-chained backbone of the hybrid polymer results decorated with antenna {Cu_2(pic)$_4$(H_2O)} subunits.

All of the dinuclear species mentioned above are new copper(II)-picolinate discrete complexes that have not been previously described in the literature. Nevertheless, the assembly modes between {Cu(pic)$_2$} fragments observed for the [Cu_2(pic)$_4$(H_2O)] moiety in **1** and **3** and the antenna {Cu_2(pic)$_4$(H_2O)} subunit in **2** are almost identical to those found in the polymeric derivatives $\{[Cu_2(pic)_3(H_2O)]X\}_n$ (X = ClO_4^-, BF_4^-) [52] and $[Cu(pic)_2]_n$ [57,58], respectively.

2.2.2. Crystal Packing of Compounds **1** and **3**

The crystal packing of **1** and **3** has a pronounced two-dimensional character with alternating hybrid and metalorganic layers stacked along the [001] direction (Figure 3). The hybrid layers consist of the $[\{XW_{12}O_{40}\}\{Cu_2(pic)_4\}]^{4-}$ chains running along the [110] direction and arranged in parallel fashion in the *xy* plane. The metalorganic sublattice contains the [Cu_2(pic)$_4$(H_2O)] dimers, all water molecules of hydration and all guanidinium cations. The interstitial water molecules do not appear to play a significant structural role as they only establish few hydrogen bonds that either connect Keggin clusters from different layers—the [Cu_2(pic)$_4$(H_2O)] dimers to the clusters or adjacent hybrid chains through the metalorganic subunits (Table S2). In contrast, the two guanidinium cations create an extended and massive network of N–H···O_{pic} hydrogen bonds with the carboxylate functionalities of the organic ligands. Each cation strongly interacts with the three crystallographically independent {Cu(pic)$_2$} fragments and arrange them in the (11–1) plane to lead to a corrugated double trihexagonal tiling of Cu^{II} atoms (Figure 4). The Keggin clusters are nested in the hexagonal motifs of this distorted Kagome-type double lattice, whereas the structure-directing guanidinium cations reside in the triangular cavities.

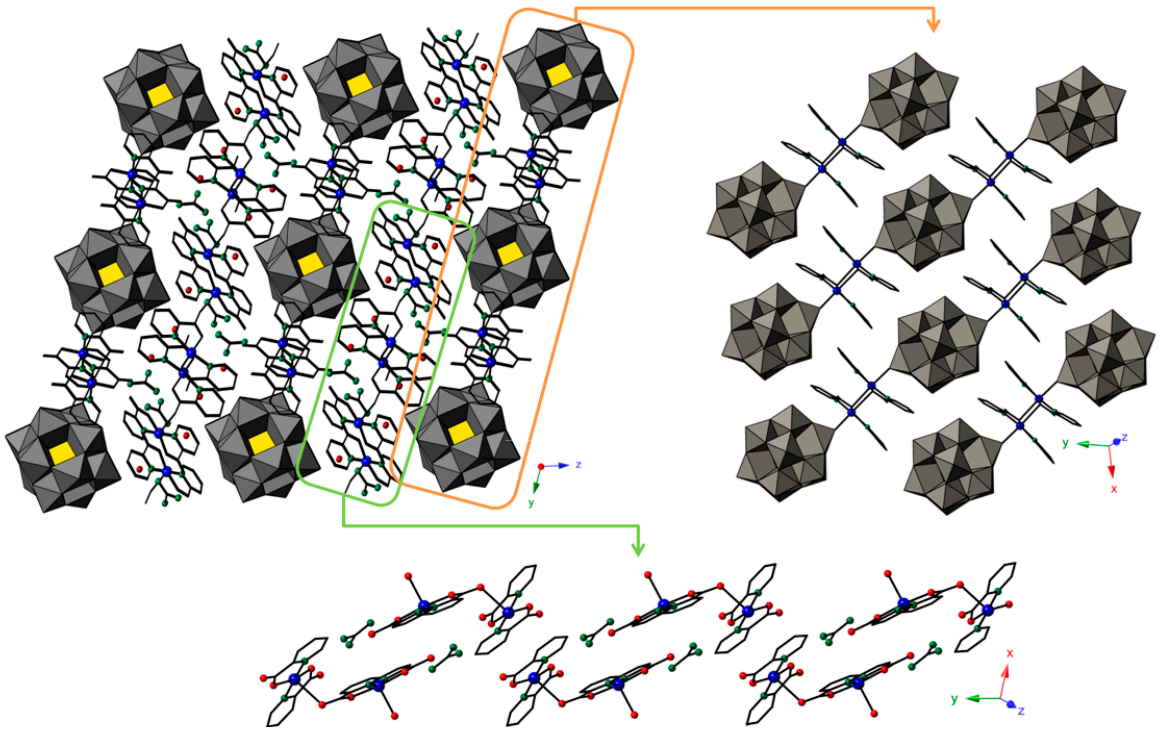

Figure 3. View of the crystal packing of **1** and **3** along the crystallographic *a* axis with details of the arrangement of the $[\{XW_{12}O_{40}\}\{Cu(pic)_2\}_2]^{4-}$ chains in the hybrid layers and the $[Cu_2(pic)_4(H_2O)]$ units and $[C(NH_2)_3]^+$ cations in the metalorganic regions.

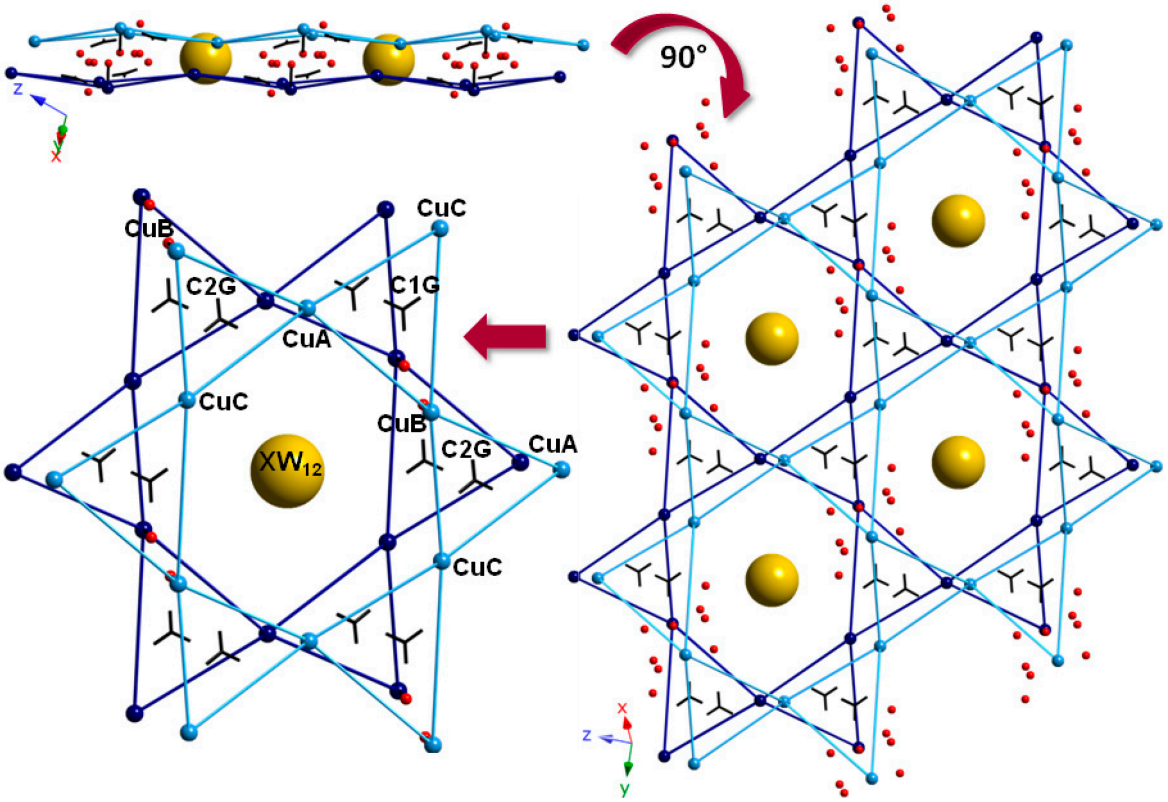

Figure 4. Schematic representation of the guanidinium-templated Kagome-type double lattice of copper(II)-picolinate complexes in **1** and **3**.

2.2.3. Crystal Packing of Compound **2**

The crystal packing of **2** shows also a two-dimensional character with hybrid layers parallel to *xy* plane (Figure 5). These layers are formed by a double sheet of Keggin clusters arranged in two levels of *z* and held together by the monomeric {CuB(pic)$_2$} and {CuC(pic)$_2$} subunits. The former link clusters lying in the same *z* level to lead to a one-dimensional assembly of alternate inorganic and metalorganic building blocks parallel to the [010] direction. The connectivity between building blocks is such that the pyridinic ring of one of the picolinate ligands is sandwiched between the tetrameric {W$_4$O$_{18}$} faces of adjacent Keggin clusters with distances between the ring centroid and the average plane of the tetramers of 2.755 and 2.856 Å. These distances are comparable to those observed in related compounds with similar POM-aromatic interactions [30,31]. The {CuC(pic)$_2$} subunits connect in turn centrosymmetrically related clusters located at different *z* levels through long Cu–O$_{POM}$ bonds typical of semi-coordination (Table 1). In this case, the two aromatic rings interact with Keggin anions as they place almost parallel to tetrameric faces of the contiguous clusters with a centroid-tetramer plane distance of 2.781 Å. The linkage through the {CuC(pic)$_2$} subunits of pairs of one-dimensional hybrid assemblies running along the crystallographic *b* axis at different *z* levels results in double-chained $[\{SiW_{12}O_{40}\}_2\{Cu(pic)_2\}_3]_n^{8n-}$ anions with rectangular cavities in the polymeric backbone and where each Keggin cluster is additionally decorated with a {Cu$_2$(pic)$_4$(H$_2$O)} dimer grafted as antenna subunit. Two of the guanidinium cations (C1G and C2G) are hosted in the rectangular cavities and they establish multiple N–H···O interactions with both the Keggin surfaces and the carboxylate groups of the picolinate ligands (Figure S3, N···O distances in the range 2.33(3)–3.28(3) Å). The layers pack with the antenna subunits directed to the interlamellar space to give rise to an alternate sequence of hybrid and metalorganic regions along the [001] direction. The antenna complexes in the metalorganic region are arranged in such a way that all picolinate ligands are almost parallel to the (10–2) plane and dimers grafted at contiguous POM sheets are hydrogen bonded by the water molecules of hydration and the guanidinium cations C3G and C4G.

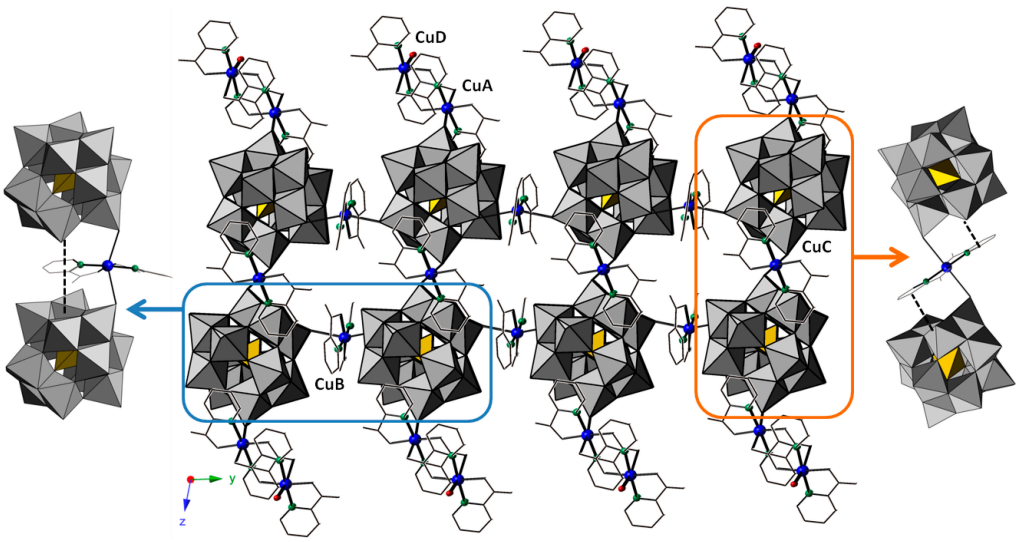

Figure 5. Projection of a $[\{SiW_{12}O_{40}\}_2\{Cu(pic)_2\}_3]_n^{8n-}$ double chain decorated with {Cu$_2$(pic)$_4$(H$_2$O)} antenna complexes on the crystallographic *bc* plane and details of the POM–aromatic interactions involving the bridging {Cu(pic)$_2$} moieties.

2.3. Thermostructural Behavior

The thermostructural behavior of the title compounds was investigated by a combination of thermal analyses and variable temperature X-ray diffraction. Thermal analyses show that all compounds decompose via three mass loss stages (Figures 6 and S4). The first stage starts at room temperature and it is associated with two endothermic processes that originate from the release of the water molecules. For **1** and **3**, the dehydration stage extends up to *ca.* 130 °C and comprises the loss of a 2.24% of the total mass, which accounts for only 6 out of the 8 water molecules determined by single-crystal X-ray diffraction (calcd. for $6H_2O$: **1**, 2.13%; **3**, 2.11%). Analogously, dehydration of **2** is completed at *ca.* 95 °C with the release of eight out of the ten water molecules determined crystallographically [calcd. (found) for $8H_2O$: 1.69% (1.71)]. It is likely that these compounds lose some weakly bound interstitial water molecules when crystals are removed from their mother liquors and filtered at room temperature prior to be analyzed thermogravimetrically. The resulting anhydrous phases all show a wide range of thermal stability, up to *ca.* 300 °C for **1** and **3** and to 280 °C in the case of **2**. Above these temperatures, the anhydrous derivatives undergo further decomposition via two highly overlapping mass loss stages. The former originates from the combination of two endothermic and one exothermic consecutive processes that can be related to the release of $[C(NH_2)_3]^+$ cations as guanidine molecules and to the combustion of part of the picolinate ligands, respectively. For **1** and **3**, this stage extends up to *ca.* 355 °C and involves the loss of a 18.22 and 18.74% of the respective total mass, which roughly corresponds to 4 cations and 6 picolinate ligands (calcd. for $4(CH_6N_3) + 6(C_6H_4NO_2)$: **1**, 4.74 + 14.45 = 19.19%; **3**, 4.70 + 14.33 = 19.03%). In the case of **2**, the upper temperature limit and the mass loss are *ca.* 380 °C and 12.10%, which roughly accounts for 4 ligands besides 8 cations (calcd. for $8(CH_6N_3) + 4(C_6H_4NO_2)$: 5.64 + 5.73 = 11.37%). The final mass loss stage originates from a complex combination of exothermic processes that must associate with the combustion of the remaining organic matter and the crumbling of the Keggin framework. The final residues are obtained at temperatures in the 530–570 °C range and have been identified as mixtures of monoclinic WO_3 (PDF 88-269) [59] and triclinic $CuWO_4$ (PDF 43-1035) with Scheelite-type structure [60] according to powder X-ray diffraction (calcd. (found) for $aCuWO_4 + bWO_3 + cXO_2$: **1**, 65.5% (65.6), $a = b = 6$, $c = 1$; **2**, 73.2% (76.1), $a = 7$, $b = 17$, $c = 2$; **3**, 65.8% (65.9), $a = b = 6$, $c = 1$).

Variable temperature powder X-ray diffraction reveals that the title compounds retain crystallinity within the range of thermal stability upon dehydration (Figures 6 and S5). For **1** and **3**, well-defined diffraction patterns are obtained up to 310 °C, which is in full agreement with the upper temperature limit of the stability range in the TGA curves. The diffraction pattern is preserved with negligible variations in the positions and intensities of the diffraction maxima for the resulting anhydrous phases (**1a** and **3a**), and this fact indicates that dehydration does not result in drastic structural changes. Compound **2** also maintains crystallinity upon dehydration, but in contrast to **1** and **3**, a phase transformation is unequivocally observed between 50 °C and 70 °C. All compounds become amorphous solids in the temperature range corresponding to the release of the guanidinium cations and the combustion of the picolinate ligands. New crystalline phases corresponding to the final residue originated upon breakdown of the Keggin framework start appearing at 510 °C and they reach complete formation at temperatures slightly beyond the end of the third mass loss stage in the TGA curves (*ca.* 590 °C).

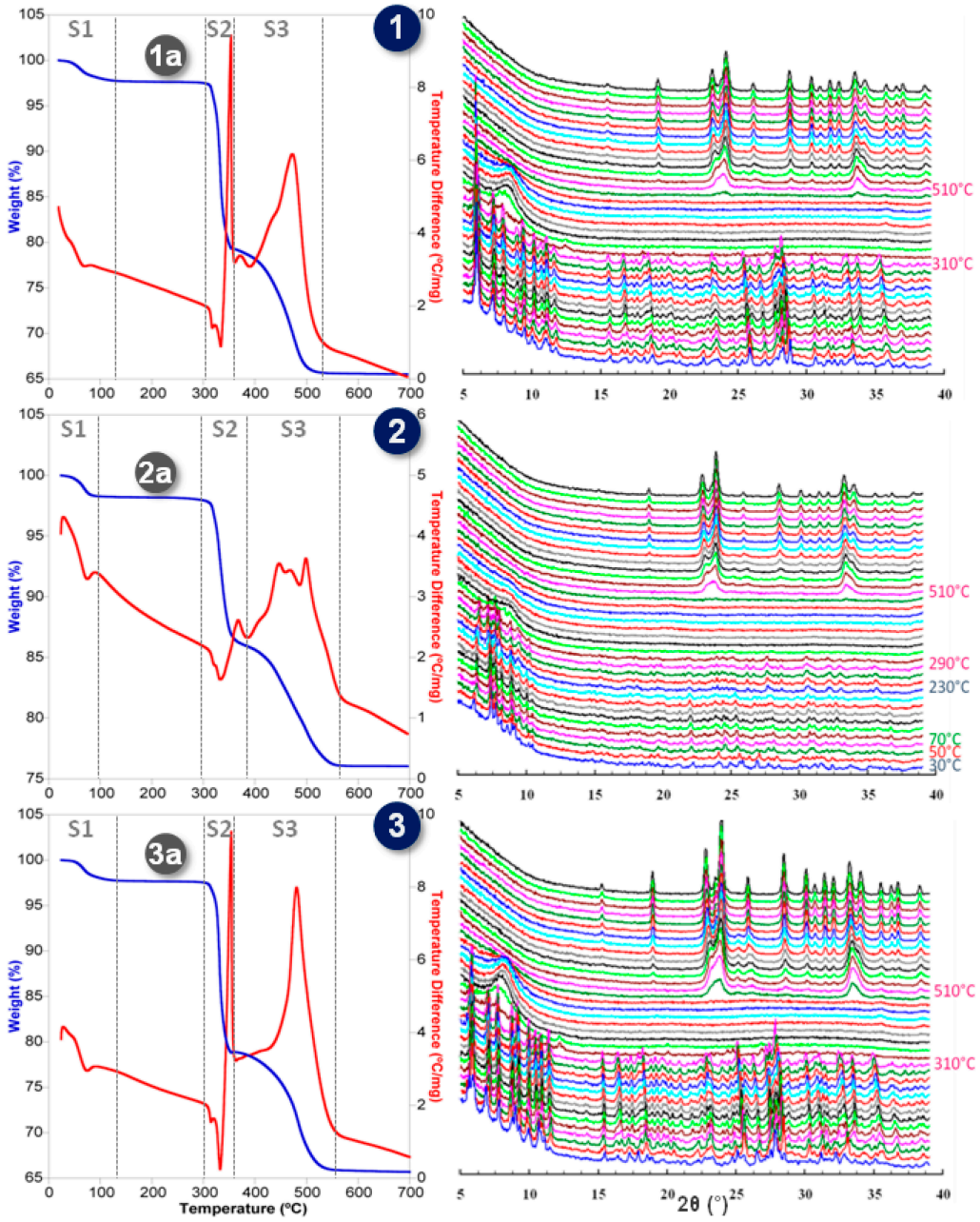

Figure 6. TGA/DTA curves and variable temperature X-ray diffraction patterns for **1**–**3**.

Analogous single-crystal X-ray diffraction studies were also carried out. Crystals of the title compounds were mounted at room temperature on a diffractometer and the temperature was raised at a rate of 1 °C min^{-1} to 140 °C for **1** and **3** and to 100 °C for **2**. The crystal of **1** preserved its integrity and crystallinity in the whole temperature range and darkening of its blue color was observed upon heating (Figure 7). This crystal stability allowed us to perform unit cell determinations at room temperature, 50, 80 and 140 °C (Table 2). In contrast, crystals of **3** cracked almost immediately after the temperature was ramped, but we could manually separate one of the resulting pieces to perform the experiment. Diffraction was of lower quality and much weaker than that observed for the isostructural **1**. Thus, the unit cell parameters determined for **3** are significantly less accurate than those of **1**, but nevertheless, they reproduce analogous trends acceptably. In the case of **2**, the laminar crystal also cracked when the temperature was ramped, but unfortunately, we could not apply

the strategy followed for **3** because the extreme fragility of the resulting pieces prevented us from their manipulation. As shown in Table 2, a significant shortening of the parameter *c* and consequent contraction of the unit cell volume is observed for both **1** and **3** when going from 80 to 140 °C, which indicates formation of the corresponding anhydrous derivatives. At this point, we lowered the temperature to 100(2) K to carry out the full data collections for both compounds and the structures of **1a** and **3a** were determined.

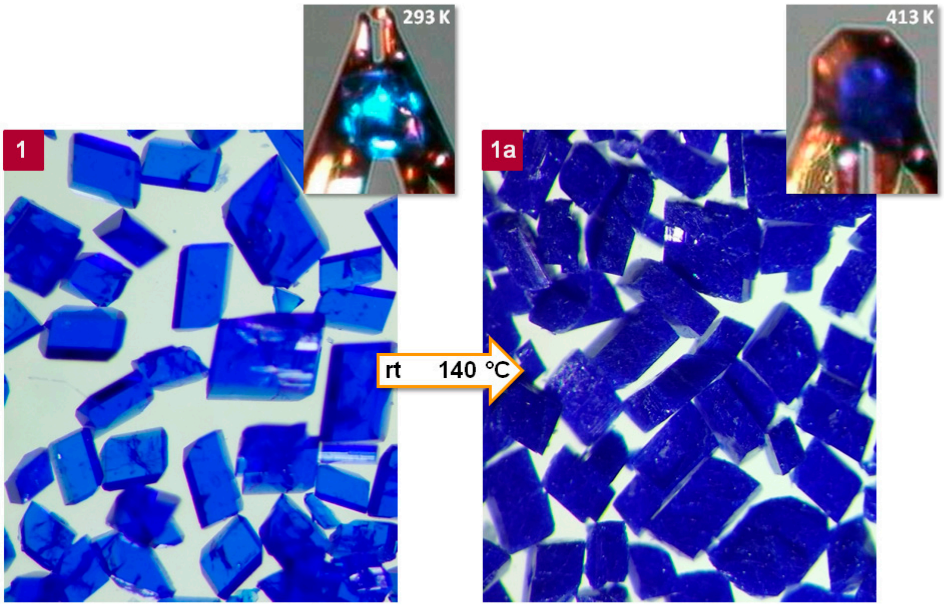

Figure 7. Photographs of single crystals of **1** taken at room temperature (left) and upon dehydration at 140 °C (right). Insets: images of the crystals used for performing the full single-crystal X-ray diffraction data collections of compouunds **1** and **1a**.

Table 2. Unit cell parameters of **1** and **3** at different temperatures.

Compounds	*T* (°C)	*a* (Å)	*b* (Å)	*c* (Å)	*α* (°)	*β* (°)	*γ* (°)	*V* (Å^3)
1	r.t	11.805(6)	16.112(6)	16.443(5)	105.65(3)	101.97(3)	91.29(4)	2936(2)
	50	11.812(5)	16.098(5)	16.356(6)	105.21(3)	101.53(4)	91.60(3)	2958(2)
	80	11.861(6)	16.077(7)	16.292(7)	104.99(4)	101.29(4)	91.85(4)	2982(2)
	140	11.818(1)	16.123(5)	16.179(7)	104.62(3)	100.18(5)	92.07(5)	2926(2)
3	r.t	11.815(4)	16.050(6)	17.047(6)	106.90(3)	94.42(3)	100.20(3)	3016(2)
	50	11.81(1)	16.05(2)	17.06(2)	106.91(9)	94.40(7)	100.09(8)	3018(5)
	80	11.88(3)	16.35(6)	16.55(5)	106.0(3)	92.9(2)	101.3(3)	3012(15)
	140	11.75(3)	15.89(4)	16.21(4)	103.4(2)	91.8(2)	100.8(2)	2882(12)
% of indexed reflections for cells at $T > 50$ °C: above 97% for **1** and below 57% for **3**								

Simple TGA/DTA experiments were performed to determine the reversibility of the dehydration processes (Figure S6). Crystalline samples of **1** and **3** were heated at a rate of 2 °C min^{-1} up to 200 °C and the so-generated anhydrous samples were exposed to the room atmosphere for one day, and then, heated again at the same rate. The recorded TGA profiles are almost identical for both heating cycles, and this fact shows that the anhydrous phases **1a** and **3a** are fully rehydrated to the original compounds simply after being in contact with moisture for a few hours. These observations were confirmed by

single-crystal X-ray diffraction. The crystals used for determining the structures of **1a** and **3a** were kept on the goniometer head in contact with the room environment and the intensity data were collected back at 100(2) K after a few days. The crystals still diffracted acceptably enough and the unit cells of the initial hydrated phases **1** and **3** were again obtained. The structural solutions were of poorer quality than those determined originally most likely due to disorder affecting the water molecules upon resorption (note the differences in the DTA profiles in Figure S6), but nevertheless, we could locate the inorganic and metalorganic building blocks in their original positions. These observations demonstrate that dehydration of both **1** and **3** proceeds via SCSC transformations, but furthermore, that this process is reversible and the anhydrous **1a** and **3a** phases also undergo SCSC transformations promoted by consequent rehydration.

*2.4. SCSC Transformations of Compounds **1** and **3** into the Anhydrous Phases **1a** and **3a***

Dehydration of compounds **1** and **3** into the phases **1a** and **3a** does not equally affect the hybrid layers and the metalorganic regions. The hybrid layers remain virtually unaltered: for example, variations in the bond lengths within the $\{CuA_2(pic)_4\}$ subunit are negligible (Table 1) and the relative arrangement of Keggin anions in the hybrid $[\{XW_{12}O_{40}\}\{Cu(pic)_2\}_2]^{4-}$ chains is only affected by a subtle lengthening of 0.1 Å in the X···X distance between adjacent clusters. In contrast, significant changes take place in the metalorganic sublattice because all water molecules of coordination and hydration reside in this area (Figure 8). Their removal promotes a reorganization of the dimeric $[Cu_2(pic)_4(H_2O)]$ moieties, each of which split into two independent $[Cu(pic)_2]$ square-planar complexes as evidenced by the remarkable lengthening of the CuB–O4C distance from *ca.* 2.49 to 3.31 Å. The contraction of the parameter *c* by 1 Å is also consequence of this splitting. While the original metalorganic regions consist in a corrugated lattice of $\{Cu(pic)_2\}$ fragments in the crystallographic *xy* plane, the release of the water molecules force the newly generated $[Cu(pic)_2]$ monomers to spread on the plane in such a way that the corrugation degree decreases and the Cu^{II} atoms become nearly coplanar. In spite of this rearrangement of complexes, the structure-directing network of N–H···O hydrogen bonds remains almost intact upon dehydration because of a slight reorientation of the guanidinium cations that preserves almost all contacts (Table S2). Thus, the double trihexagonal tiling described above is maintained without noticeable alterations (Figure 9).

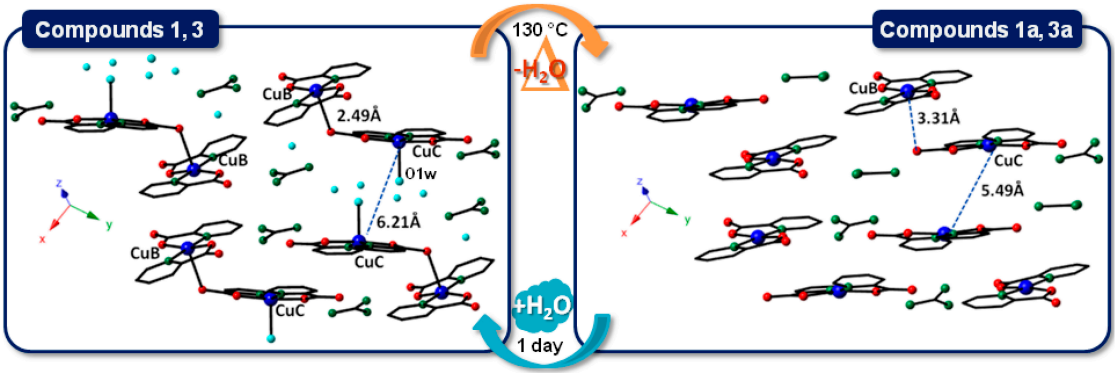

Figure 8. Arrangement of $\{Cu(pic)_2\}$ fragments and $[C(NH_2)_3]^+$ cations in the metalorganic region of **1** and **3** compared to that found in the anhydrous phases **1a** and **3a**. Note the splitting of the dimer $[Cu_2(pic)_4(H_2O)]$ into monomers upon dehydration.

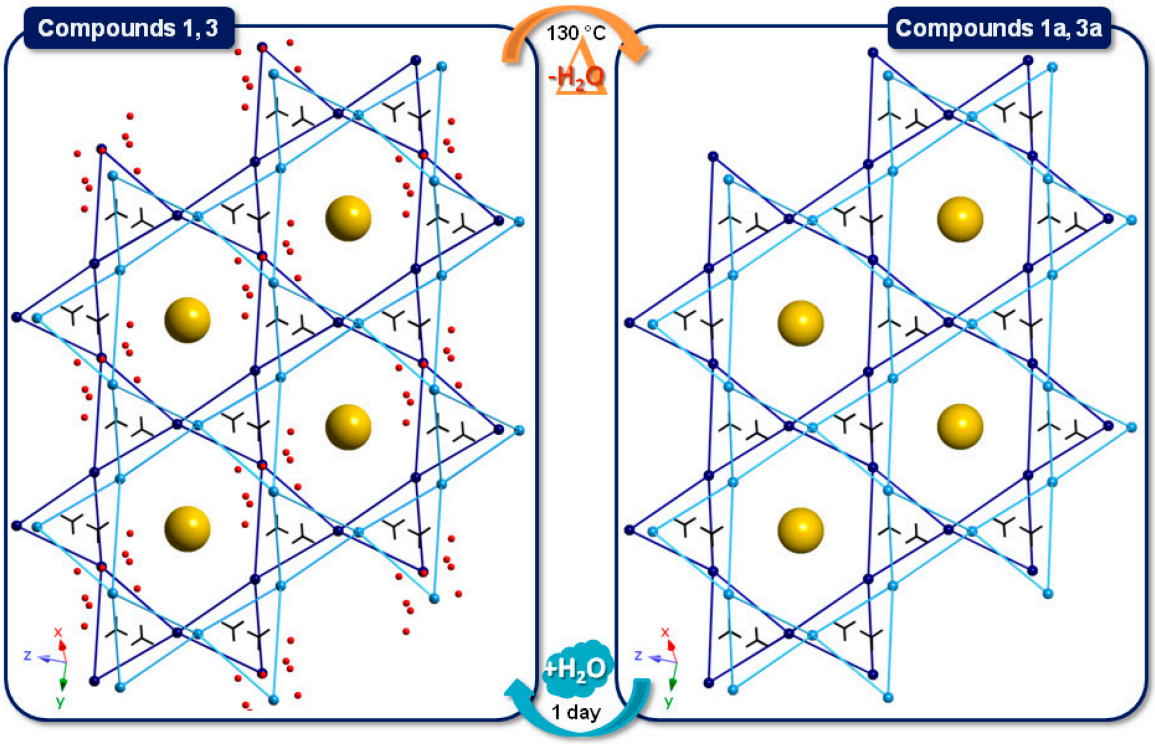

Figure 9. Guanidinium-templated Kagome-type double lattice of Cu^{II} atoms in **1** and **3** compared to that found in the anhydrous phases **1a** and **3a**.

*2.5. Electron Paramagnetic Resonance Spectroscopy for Compounds **1** and **1a***

The EPR spectra of **1** (Figure 10) and **3** (Figure S7) are virtually identical in good agreement with the isostructurality of the compounds. The only difference worth to be mentioned is the largest line width observed for **3**, which is likely due to the lower crystallinity of this compound when compared to **1**. The spectra are relatively complex as a result of the overlapping of the contributions from the different copper(II)-picolinate dimeric entities coexisting in the crystal packing. The X-band spectra show multiple resonances in the range 2300–3800 Gauss and a half-field signal corresponding to the $\Delta M_S = \pm 2$ forbidden transition centered at *ca.* 1600 Gauss, which indicates the presence of a magnetically isolated triplet state ($S = 1$). Moreover, a partially resolved hyperfine structure originating from the interaction of an electron spin with a limited number of non-zero nuclear spins is also observed in both spectra. The number of detectable lines in this hyperfine structure is above the 4 lines that would correspond to a spin doublet interacting with a single $I = 3/2$ nucleus and this confirms the presence of an isolated $S = 1$ state. Both the X- and Q-band spectra display at least one signal for which the apparent g value is substantially lower than that of the free electron (3600 and 12200 Gauss, respectively). As all Cu^{II} atoms in **1** and **3** are in octahedral or square-pyramidal coordination environments, the presence of such signals can only be attributed to a noticeable zero-field splitting (ZFS) within a multiplet state.

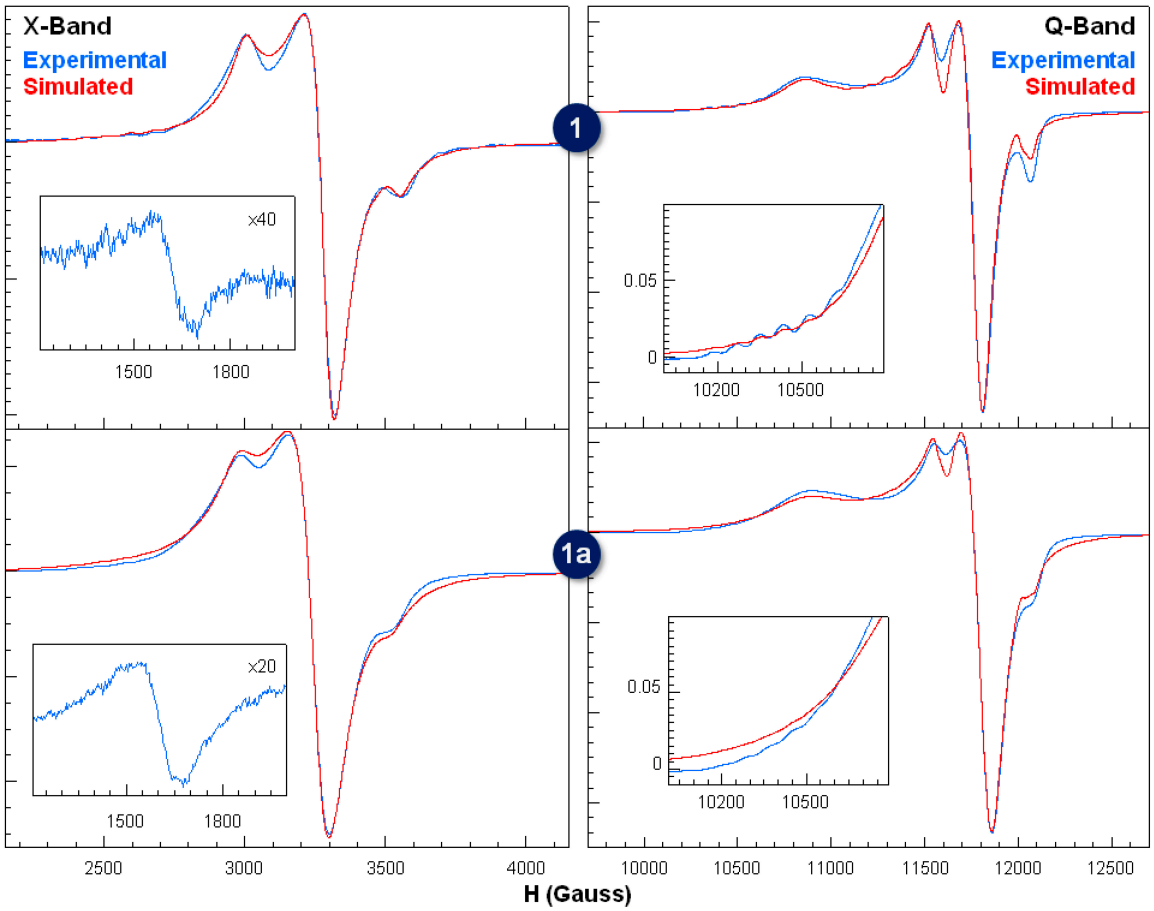

Figure 10. Experimental and simulated X-band (υ = 9.49 GHz) and Q-band (υ = 34.05 GHz) EPR spectra of **1** and **1a** at room temperature.

The observation of such multiplet states can be well correlated with the coexistence of the dinuclear entities {$Cu_2(pic)_4$} and [$Cu_2(pic)_4(H_2O)$]. In both complexes, intradimeric magnetic exchange takes place through axial-equatorial pathways: μ^2-O bridging atoms for {$Cu_2(pic)_4$} and O–C–O linkages in the case of [$Cu_2(pic)_4(H_2O)$]. The spectroscopic features suggest that the former are magnetically isolated by the bulky diamagnetic Keggin clusters and give rise to a common signal with the typical features of a triplet state with significant zero-field splitting, whereas the latter are coupled in an extended system of long-range, weak magnetic interactions that average their individual signals. Thus, the spectra were initially simulated as the sum of the following individual contributions: one signal of axial symmetry corresponding to a cooperative exchange **g** tensor (signal 1) and another signal originating from an $S = 1$ spin state with collinear **D** and **g** tensors of axial symmetry (Figure S8). The fit of signal 1 to the experimental profile was improved by breaking the axial symmetry with some equatorial anisotropy, whereas that of signal 2 required the introduction of certain ZFS also in the equatorial plane. The value of the parameter E used during the fitting should be considered only as a simple approximation or as a maximum value for the equatorial ZFS effect.

The calculated spin Hamiltonian parameters are shown in Table 3, together with those of the isostructural **3** and the anhydrous derivative **1a**. The g values are consistent with those expected for the topology shown by the copper(II) chromophores in the title compounds and confirms that the ground state is mainly of $d(x^2–y^2)$ type. Therefore, the intradimeric coupling interactions must be

very small in both cases considering the axial-equatorial pathways. The calculated hyperfine coupling constant (87×10^{-4} cm^{-1}) is actually half of that expected for a Cu^{II} chromophore with g = 2.25 and N_2O_2-type equatorial plane, which implies that each unpaired electron must interact with the nuclear spins of two different Cu^{II} ions as corresponds to the presence of magnetically isolated dinuclear entities. The D parameter obtained is relatively small and this fact is in good agreement with the strong deviation of the axial component of the **g** tensors with respect to the intradimeric Cu–Cu axis, which reduces the anisotropic exchange contribution.

Table 3. Spin Hamiltonian parameters g, A, D and E ($\times10^{-4}$ cm^{-1}) for compounds **1**, **1a**, **2** and **3**.

Compounds	signal 1				signal 2				
	g_1	g_2	$g_\perp$	$g_3 = g_\parallel$	$g_\perp$	$g_\parallel$	A	D	E
1	2.061(1)	2.073(1)	2.067(1)	2.243(2)	2.061(1)	2.240(1)	87(1)	450(5)	20(5)
1a	2.056(1)	2.068(1)	2.062(1)	2.246(2)	2.061(1)	2.240(1)	87(1)	430(5)	20(5)
3	2.062(1)	2.071(1)	2.066(1)	2.243(2)	2.060(1)	2.240(1)	87(1)	450(5)	20(5)
2	-	-	2.063(1)	2.251(2)	2.060(2)	2.236(2)	88(3)	470(5)	-

Dehydration of **1** into **1a** does not significantly affect the EPR spectra in spite of the fact that the release of the water molecules results in the splitting of one of the dimeric entities into independent monomers with consequent modification of the coordination geometry around the Cu^{II} centers from square-pyramidal to square-planar. The two main contributions corresponding to the isolated dimer and the extended system can still be well appreciated in the spectra of **1a**. For the former, the lines of the fine structure approach each other due to a decrease of the D parameter that may associate with a reduction of the anisotropy around the CuA centers. All of the fine and hyperfine lines become wider, resulting in a loss of resolution that might a priori be related to an increase of dipolar interactions or to a reduction of the exchange coupling. However, we believe that this phenomenon is simply due to a loss of crystallinity in the solid sample upon heating the starting material in an oven. It is worth highlighting that EPR spectroscopy finely demonstrates that rehydration of **1a** into the initial **1** is fully achieved in a very short time under standard atmospheric conditions. Using a freshly prepared sample of **1a**, the original experimental profiles of **1** were recovered within a few minutes when an open sample holder was used, but fortunately, sealing the latter slowed the process down enough for allowing us to collect the spectra of the anhydrous derivative.

Figure 11 displays the X-band (9.40 GHz) and Q-band (34.10 GHz) EPR spectra of **2** recorded at room temperature on a grained polycrystalline sample. The spectra are closely related to those of **1** and **3** as contributions of two different magnetic systems are also observed: a magnetically isolated S = 1 state with significant zero-field splitting and a poorly resolved hyperfine structure in the parallel region and a more intense rhombic signal that must originate from a cooperative exchange **g** tensor after considering its lack of hyperfine lines. The calculated g, A and D values are similar to those determined for **1** and **3** (Table 3). Taking into account the structural features of **2**, it should be assumed that the signal of the isolated triplet state corresponds to the dinuclear $\{Cu_2(pic)_4(H_2O)\}$ antenna subunits, and hence the rhombic signal must then be ascribed to the presence of long-range, weak magnetic interactions involving the monomeric $\{Cu(pic)_2\}$ bridging subunits. Therefore, magnetic

exchange pathways between the CuB and CuC ions must exist through the Keggin clusters, or most likely, through the strong N–H···O hydrogen bonds established with the guanidiniums cations.

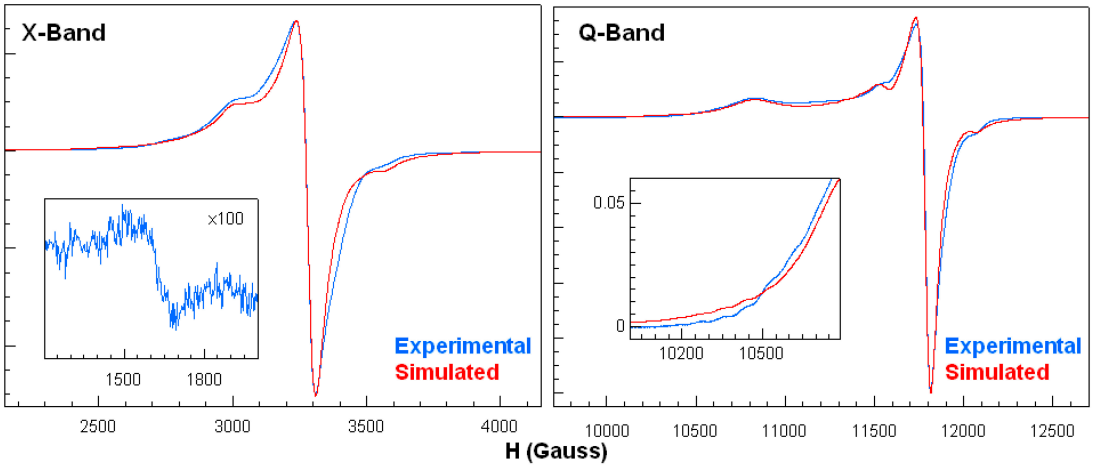

Figure 11. Experimental and simulated X-band (υ = 9.49 GHz) and Q-band (υ = 34.06 GHz) EPR spectra of **2** at room temperature.

3. Experimental Section

3.1. Materials and Methods

The precursors $K_8[\alpha\text{-}SiW_{11}O_{39}]\cdot 13H_2O$ and $K_8[\alpha\text{-}GeW_{11}O_{39}]\cdot 13H_2O$ were prepared according to the literature [61,62] and identified by IR spectroscopy. All other chemicals were obtained from commercial sources and used without further purification. Carbon, hydrogen, and nitrogen were determined on a Perkin-Elmer 2400 CHN analyzer (Perkin Elmer, Waltham, MA, USA). Infrared spectra for solid samples were obtained as KBr pellets on a SHIMADZU FTIR-8400S spectrometer (Shimadzu, Kyoto, Japan). Thermogravimetric and Differential Thermal Analyses were carried out from room temperature to 750 °C at a rate of 5 °C min^{-1} on a TA Instruments 2960 SDT thermobalance (TA Instruments, New Castle, DE, USA) under a 100 $cm^3\cdot min^{-1}$ flow of synthetic air. Electron Paramagnetic Resonance (EPR) spectra were recorded on Bruker ELEXSYS 500 (superhigh-Q resonator ER-4123-SHQ, (Bruker, Karlsruhe, Germany) and Bruker EMX (ER-510-QT resonator, Bruker, Karlsruhe, Germany) continuous wave spectrometers for Q- and X- bands, respectively.

*3.2. Synthesis of $[C(NH_2)_3]_4[\{SiW_{12}O_{40}\}\{Cu_2(pic)_4\}]\cdot[Cu_2(pic)_4(H_2O)]_2\cdot 6H_2O$ (**1**) and $[C(NH_2)_3]_8[\{SiW_{12}O_{40}\}_2\{Cu(pic)_2\}_3\{Cu_2(pic)_4(H_2O)\}_2]\cdot 8H_2O$ (**2**)*

To a solution of $K_8[\alpha\text{-}SiW_{11}O_{39}]\cdot 13H_2O$ (322 mg, 0.10 mmol) in water (30 mL), $CuCl_2\cdot 2H_2O$ (17 mg, 0.10 mmol) was added. After stirring the reaction mixture at room temperature for 30 min, picolinic acid (24 mg, 0.20 mmol) was added. The resulting solution was stirred for one additional hour and then aqueous 1M guanidinium chloride (1 mL) was added dropwise. A mixture of prismatic blue crystals of **1** as the major fraction and laminar blue crystals of **2** as a side product was obtained

upon slow evaporation of the final solution for *ca.* five days. The two compounds were manually separated using an optical microscope for their full characterization and structural determination.

Compound **1**. Yield: 32% based on W. Elemental Analyses (%): Calcd. (found) for $C_{76}H_{88}Cu_6N_{24}O_{72}SiW_{12}$: C, 17.88 (18.02); H, 1.74 (1.70); N, 6.58 (6.57). IR (cm^{-1}): 3379 s, 2924 w, 2853 w, 1645 vs, 1603 s, 1572 s, 1478 m, 1447 w, 1362 s, 1350 s, 1292 m, 1265 w, 1167 w, 1096 w, 1051 m, 1015 w, 970 m, 924 vs, 883 m, 853 m, 804 vs, 758 s, 712 m, 694 m, 660 m, 525 m, 457 w.

Compound **2**. Yield: less than 5% based on W. Elemental Analyses (%): Calcd. (found) for $C_{92}H_{124}Cu_7N_{38}O_{118}Si_2W_{24}$: C, 12.9 (13.22); H, 1.45 (1.43); N, 6.21 (6.34). IR (cm^{-1}): 3366 s, 2926 w, 2853 w, 1642 vs, 1603 s, 1570 s, 1476 m, 1449 w, 1364 s, 1350 s, 1290 m, 1263 w, 1165 w, 1096 w, 1051 m, 1015 w, 970 m, 922 vs, 883 m, 854 m, 800 vs, 754 s, 712 m, 693 m, 660 m, 523 m, 455 w.

*3.3. Synthesis of $[C(NH_2)_3]_4[\{GeW_{12}O_{40}\}\{Cu_2(pic)_4\}]\cdot[Cu_2(pic)_4(H_2O)]_2\cdot 6H_2O$ (**3**)*

The synthetic procedure above was followed but for using a solution of $K_4[\alpha\text{-}GeW_{11}O_{39}]\cdot 13H_2O$ (329 mg, 0.10 mmol) in water (20 mL). Prismatic blue crystals of **3** suitable for X-ray diffraction were obtained as a single solid phase by slow evaporation of the final solution for *ca.* 5 days. Yield: 31% based on W. Elemental Analyses (%): Calcd. (found) for $C_{76}H_{88}Cu_6GeN_{24}O_{72}W_{12}$: C, 17.73 (18.05); H, 1.72 (1.60); N, 6.53 (6.94). IR (cm^{-1}): 3370 s, 2924 w, 2853 w, 1642 vs, 1603 s, 1570 s, 1478 m, 1445 w, 1367 s, 1350 s, 1290 m, 1263 w, 1165 w, 1094 w, 1051 m, 966 s, 883 vs, 853 m, 831 s, 787 vs, 754 s, 712 m, 692 m, 660 m, 557 w, 461 s.

3.4. X-ray Crystallography

Crystallographic data for **1**–**3** and the anhydrous phases **1a** and **3a** are given in Table 4. Intensity data were collected at 100(2) K on an Agilent Technologies SuperNova diffractometer (Santa Clara, CA, USA) equipped with an Oxford Cryostream 700 PLUS temperature device (Oxford, UK). Mirror-monochromated Mo Kα radiation (λ = 0.71073 Å) and an Eos CCD detector (Santa Clara, CA, USA) was used in all cases with the exception of **1** and **3a**, for which data collection involved mirror-monochromated Cu Kα radiation (λ = 1.5418 Å) and an Atlas CCD detector (Santa Clara, CA, USA). In the case of the anhydrous phases **1a** and **3a**, a single crystal of the corresponding hydrated compound was mounted on the goniometer and a preliminary data collection was performed at room temperature to check that its diffraction was of sufficient quality. The temperature was then ramped at a rate of 2 K min^{-1} and unit cell measurements were carried out at 323, 353 and 413(2) K to ensure whether the sample maintained its integrity as a single crystal during the structural transformation associated to dehydration. Once the temperature reached 413(2) K, it was lowered to 100(2) K at a rate of 6 K min^{-1} for performing a full data collection of the so generated anhydrous phases. The crystals were kept on the goniometer head and exposed to room atmosphere for several days, after which routine full data collections corresponding to the initial hydrated forms were carried out at 100(2) K.

Table 4. Crystallographic data for **1**–**3** and for the anhydrous phases **1a** and **3a**.

Parameters	1	1a	2	3	3a
Formula	$C_{76}H_{88}Cu_6N_{24}O_{72}SiW_{12}$	$C_{76}H_{72}Cu_6N_{24}O_{64}SiW_{12}$	$C_{92}H_{124}Cu_7N_{38}O_{118}Si_2W_{24}$	$C_{76}H_{88}Cu_6GeN_{24}O_{72}W_{12}$	$C_{76}H_{72}Cu_6GeN_{24}O_{64}W_{12}$
Fw (g mol^{-1})	5105.2	4961.1	8563.6	5149.7	5005.6
Crystal system	triclinic	triclinic	triclinic	triclinic	triclinic
Space group	*P*–1	*P*–1	*P*–1	*P*–1	*P*–1
a (Å)	11.7014(4)	11.6039(3)	11.9426(2)	11.7110(3)	11.6025(7)
b (Å)	15.9523(5)	15.9379(5)	12.8151(3)	15.9628(6)	15.9736(9)
c (Å)	17.0285(5)	15.9984(5)	30.0533(6)	17.0341(5)	15.9849(10)
α (°)	107.102(3)	104.292(3)	101.508(2)	107.057(3)	104.371(5)
β (°)	94.393(3)	91.168(2)	90.346(2)	94.372(2)	91.222(5)
γ (°)	101.008(3)	100.599(2)	105.544(2)	100.971(2)	100.534(5)
V (Å^3)	2952.2(2)	2811.6(1)	4333.6(2)	2958.9(2)	2814.5(3)
Z	1	1	1	1	1
ρ_{calcd} (g cm^{-3})	2.872	2.930	3.281	2.890	2.953
μ (mm^{-1})	23.180	13.447	16.822	13.025	24.412
Reflections:					
Collected	22568	19291	34946	19292	20323
Unique	11493	11071	17052	11018	10854
Observed [$I > 2\sigma(I)$]	10892	10022	15317	10485	7649
R_{int}	0.032	0.021	0.023	0.022	0.049
Parameters	514	494	788	518	494
$R(F)$ [a] [$I > 2\sigma(I)$]	0.050	0.046	0.086	0.044	0.079
$wR(F^2)$ [a] [all data]	0.117	0.085	0.176	0.093	0.231
GoF	1.278	1.363	1.273	1.280	1.039

[a] $R(F) = \Sigma||F_o|-|F_c||/\Sigma|F_o|$; $wR(F^2) = \{\Sigma[w(F_o^2-F_c^2)_2]/\Sigma[w(F_o^2)^2]\}^{1/2}$.

Data frames were processed (unit cell determination, intensity data integration, correction for Lorentz and polarization effects, and analytical absorption correction with face indexing) using the CrysAlis Pro software package (Agilent Technologies UK Ltd., Oxford, UK) [63]. The structures were solved using OLEX (OlexSys Ltd in Durham University, Durham, UK) [64] and refined by full-matrix least-squares with SHELXL-97 (University of Goettingen, Goettingen, Germany) [65]. Final geometrical calculations were carried out with PLATON (Utrecht University, Utrecht, The Netherlands) [66] as integrated in WinGX (University of Glasgow, Glasgow, UK) [67]. Thermal vibrations were treated anisotropically for heavy atoms (W, Cu, Si). Hydrogen atoms of the organic ligands were placed in calculated positions and refined using a riding model with standard SHELXL parameters. In all cases, the Keggin clusters displayed disorder originated from slight tilting in the crystal packing. This tilting was modeled by disordering the O atoms of the Keggin clusters over two positions labeled as O/OZ. The population factor within the O/OZ pairs was initially refined as a single free variable, resulting in the following occupancies: 50/50 for **1**, 48/52 for **1a**, 65/35 for **2**, 51/49 for **3** and 52/48 for **3a**. CCDC-1058791 (**1**), -1058793 (**2**), -1058794 (**3**), -1058792 (**1a**), and -1058795 (**3a**) contain the supplementary crystallographic data for this paper. These data

can be obtained free of charge from The Cambridge Crystallographic Data Centre via www.ccdc.cam.ac.uk/data_request/cif.

Powder X-ray diffraction patterns were collected on a Bruker D8 Advance diffractometer (Karlsruhe, Germany) operating at 30 kV and 20 mA and equipped with a Pt sample holder, Cu tube (λ = 1.5418 Å), Vantec-1 PSD detector (Karlsruhe, Germany), and Anton Parr HTK2000 high-temperature furnace (Graz, Austria). The patterns were recorded in 2θ steps of 0.033° in the $5 \leq 2\theta \leq 39°$ range using an exposure time of 0.3 s per step. Full data sets were recorded from 30 to 770 °C every 20 °C and a heating rate of 0.16 °C s^{-1} was applied between the temperatures.

4. Conclusions

The study presented herein represents a good indication of the fact that single-crystal to single-crystal transformations might be a common structural response to thermal dehydration in a wide scope of hybrid compounds composed of polyoxometalate anions and transition metal complexes bearing organic ligands. To date, such types of solid-state phase transition studies have only been developed for polyoxometalate-based hybrid compounds containing bis(aminopyridyl)-type ligands. In this work, we demonstrate that analogous behavior can also be found in related systems with completely different metalorganic subunits such as transition metal bis(picolinate) complexes. The aiding role of guanidinium cations as structure-directing agents appears to be a key factor in facilitating the crystal transformations because they are able to establish a massive network of intermolecular interactions that remains nearly unaltered upon dehydration.

Acknowledgments

This work was funded by Eusko Jaurlaritza/Gobierno Vasco (grant IT477-10 and predoctoral fellowship to A.P.), Ministerio de Economía y Competitividad (grant MAT2013-48366-C2-2P) and Universidad del País Vasco UPV/EHU (grant UFI11/53). Technical and human support provided by SGIker (UPV/EHU) is gratefully acknowledged.

Author Contributions

A.P. prepared the title compounds, performed their physicochemical characterization and analyzed the structures in close collaboration with A.I.; L.S.F. collected the single-crystal X-ray diffraction data and solved the structures; S.R. carried out the thermal analyses and prepared the manuscript; L.L. was in charge of collecting and interpreting the EPR spectra; and J.M.G.-Z. conceived the work and acted as the scientific coordinator together with L.L.

Conflicts of Interest

The authors declare no conflict of interest.

References

1. Reinoso, S.; Vitoria, P.; Gutiérrez-Zorrilla, J.M.; Lezama, L.; San Felices, L.; Beitia, J.I. Inorganic-Metalorganic Hybrids Based on Copper(II)-Monosubstituted Keggin Polyanions and Dinuclear Copper(II)-Oxalate Complexes. Synthesis, X-ray Structural Characterization, and Magnetic Properties. *Inorg. Chem*. **2005**, *44*, 9731–9742.
2. Reinoso, S.; Vitoria, P.; Gutiérrez-Zorrilla, J.M.; Lezama, L.; Madariaga, J.M.; San Felices, L.; Iturrospe, A. Coexistence of Five Different Copper(II)-Phenanthroline Species in the Crystal Packing of Inorganic-Metalorganic Hybrids Based on Keggin Polyoxometalates and Copper(II)-Phenanthroline-Oxalate Complexes. *Inorg. Chem.* **2007**, *46*, 4010–4021.
3. Zhang, Z.; Yang, J.; Liu, Y.-Y.; Ma, J.-F. Five Polyoxometalate-Based Inorganic-Organic Hybrid Compounds Constructed by a Multidentate N-Donor Ligand: Syntheses, Structures, Electrochemistry, and Photocatalysis Properties. *CrystEngComm* **2013**, *15*, 3843–3853.
4. Aoki, S.; Kurashina, T.; Kasahara, Y.; Nishijima, T.; Nomiya, K. Polyoxometalate (POM)-Based, Multi-Functional, Inorganic-Organic, Hybrid Compounds: Syntheses and Molecular Structures of Silanol- and/or Siloxane Bond-Containing Species Grafted on Mono- and Tri-Lacunary Keggin POMs. *Dalton Trans.* **2011**, *40*, 1243–1253.
5. Bai, Y.; Zhang, G.-Q.; Dang, D.-B.; Ma, P.-T.; Gao, H.; Niu, J.-Y. Assembly of Polyoxometalate-Based Inorganic-Organic Compounds from Silver-Schiff Base Building Blocks: Synthesis, Crystal Structures and Luminescent Properties. *CrystEngComm* **2011**, *13*, 4181–4187.
6. Dolbecq, A.; Dumas, E.; Mayer, C.R.; Mialane, P. Hybrid Organic-Inorganic Polyoxometalate Compounds: From Structural Diversity to Applications. *Chem. Rev.* **2010**, *110*, 6009–6048.
7. Liu, B.; Yu, Z.-T.; Yang, J.; Hua, W.; Liu, Y.-Y.; Ma, J.-F. First Three-Dimensional Inorganic-Organic Hybrid Material Constructed From an "Inverted Keggin" Polyoxometalate and a Copper(I)-Organic Complex. *Inorg. Chem.* **2011**, *50*, 8967–8972.
8. Zheng, L.M.; Wang, Y.S.; Wang, X.Q.; Korp, J.D.; Jacobson, A.J. Anion-Directed Crystallization of Coordination Polymers: Syntheses and Characterization of $Cu_4(2\text{-pzc})_4(H_2O)_8(Mo_8O_{26})\cdot 2H_2O$ and $Cu_3(2\text{-pzc})_4(H_2O)_2(V_{10}O_{28}H_4)\cdot 6.5H_2O$ (2-pzc = 2-Pyrazinecarboxylate). *Inorg. Chem.* **2001**, *40*, 1380–1385.
9. Hagrman, D.; Hagrman, P.J.; Zubieta, J. Solid-State Coordination Chemistry: The Self-Assembly of Microporous Organic-Inorganic Hybrid Frameworks Constructed from Tetrapyridylporphyrin and Bimetallic Oxide Chains or Oxide Clusters. *Angew. Chem.* **1999**, *38*, 3165–3168.
10. Lu, Y.; Xu, Y.; Wang, E.B.; Lü, J.; Hu, C.W.; Xu, L. Novel Two-Dimensional Network Constructed from Polyoxomolybdate Chains Linked through Copper-Organonitrogen Coordination Polymer Chains: Hydrothermal Synthesis and Structure of $[H_2bpy][Cu(4,4'\text{-bpy})]_2[HPCuMo_{11}O_{39}]$. *Cryst. Growth Des.* **2005**, *5*, 257–260.
11. Shivaiah, V.; Nagaraju, M.; Das, S.K. Formation of a Spiral-Shaped Inorganic-Organic Hybrid Chain, $[Cu^{II}(2,2'\text{-bipy})(H_2O)_2Al(OH)_6Mo_6O_{18}]_n^{n-}$: Influence of Intra- and Interchain Supramolecular Interactions. *Inorg. Chem.* **2003**, *42*, 6604–6606.
12. Yao, S.; Yan, J.-H.; Duan, H.; Zhang, Z.-M.; Li, Y.-G.; Han, X.-B.; Shen, J.-Q.; Fu, H.; Wang, E.-B. Integration of Ln-Sandwich POMs into Molecular Porous Systems Leading to Self-Assembly of Metal-POM Framework Materials. *Eur. J. Inorg. Chem*. **2013**, 4770–4774.

13. Kong, X.J.; Ren, Y.-P.; Zheng, P.-Q.; Long, Y.-X.; Long, L.-S.; Huang, R.-B.; Zheng, L.-S. Construction of Polyoxometalates-Based Coordination Polymers through Direct Incorporation between Polyoxometalates and the Voids in a 2D Network. *Inorg. Chem*. **2006**, *45*, 10702–10711.
14. Khan, M.I.; Yohannes, E.; Doedens, R.J. A Novel Series of Materials Composed of Arrays of Vanadium Oxide Container Molecules, $[V_{18}O_{42}(X)]$ (X = H_2O, Cl^-, Br^-): Synthesis and Characterization of $[M_2(H_2N(CH_2)_2NH_2)_5][(M(H_2N(CH_2)_2NH_2)_2]_2V_{18}O_{42}(X)]\cdot 9H_2O$ (M = Zn, Cd). *Inorg. Chem*. **2003**, *42*, 3125–3129.
15. An, H.Y.; Wang, E.B.; Xiao, D.R.; Li, Y.G.; Su, Z.M.; Xu, L. Chiral 3D Architectures with Helical Channels Constructed from Polyoxometalate Clusters and Copper-Amino Acid Complexes. *Angew. Chem.* **2006**, *45*, 904–908.
16. Dai, L.M.; You, W.S.; Wang, E.B.; Wu, S.X.; Su, Z.M.; Du, Q.H.; Zhao, Y.; Fang, Y. Two Novel One-Dimensional α-Keggin-Based Coordination Polymers with Argentophilic $\{Ag_3\}^{3+}/\{Ag_4\}^{4+}$ Clusters. *Cryst. Growth Des.* **2009**, *9*, 2110–2116.
17. Darling, K.; Smith, T.M.; Vargas, J.; O'Connor, C.J.; Zubieta, J. Polyoxometalate Clusters as Building Blocks for Oxide Materials: Synthesis and Structure of a Three-dimensional Copper-Pyrazinetetrazolate / Keggin Assembly. *Inorg. Chem. Commun.* **2013**, *32*, 1–4.
18. Hao, X.-L.; Ma, Y.-Y.; Wang, Y.-H.; Zhou, W.-Z.; Li, Y.-G. New Organic-Inorganic Hybrid Assemblies based on Metal-bis(betaine) Coordination Complexes and Keggin-type Polyoxometalates. *Inorg. Chem. Commun*. **2014**, *41*, 19–24.
19. Li, S.; Ma, H.; Pang, H.; Zhang, Z.; Yu, Y.; Liu, H.; Yu, T. Tuning the Dimension of POM-Based Inorganic-Organic Hybrids from 3D Self-Penetrating Framework to 1D Poly-Pendant Chain via Changing POM Clusters and Introducing Secondary Spacers. *CrystEngComm* **2014**, *16*, 2045–2055.
20. Henry, N.; Costenoble, S.; Lagrenee, M.; Loiseau, T.; Abraham, F. Lanthanide-Based 0D and 2D Molecular Assemblies with the Pyridazine-3,6-dicarboxylate Linker. *CrystEngComm* **2011**, *13*, 251–258.
21. Wang, X.; Qin, C.; Wang, E.; Li, Y.; Hao, N.; Hu, C.; Xu, L. Syntheses, Structures, and Photoluminescence of a Novel Class of d^{10} Metal Complexes Constructed from Pyridine-3,4-dicarboxylic Acid with Different Coordination Architectures. *Inorg. Chem.* **2004**, *43*, 1850–1856.
22. Cepeda, J.; Beobide, G.; Castillo, O.; Luque, A.; Pérez-Yánez, S.; Román, P. Structure-Directing Effect of Organic Cations in the Assembly of Anionic In(III)/Diazinedicarboxylate Architectures. *Cryst. Growth Des*. **2012**, *12*, 1501–1512.
23. Pinar, A.B.; Gómez-Hortiguela, L.; McCusker, L.B.; Pérez-Pariente, J. Controlling the Aluminum Distribution in the Zeolite Ferrierite via the Organic Structure Directing Agent. *Chem. Mater*. **2013**, *25*, 3654–3661.
24. Van Bommel, K.J.C.; Friggeri, A.; Shinkai, S. Organic Templates for the Generation of Inorganic Materials. *Angew. Chem.* **2003**, *42*, 980–999.
25. Decker, R.; Schlickum, U.; Klappenberger, F.; Zoppellaro, G.; Klyatskaya, S.; Ruben, M.; Barth, J.V.; Brune, H. Using Metal-Organic Templates to Steer the Growth of Fe and Co Nanocluster. *Appl. Phys. Lett*. **2008**, *93*, 243102 / 1–243102 / 3.

26. Abrahams, B.F.; Hawley, A.; Haywood, M.G.; Hudson, T.A.; Robson, R.; Slizys, D.A. Serendipity and Design in the Generation of New Coordination Polymers: An Extensive Series of Highly Symmetrical Guanidinium-Templated, Carbonate-Based Networks with the Sodalite Topology. *J. Am. Chem. Soc.* **2004**, *126*, 2894–2904.
27. Reinoso, S.; Dickman, M.H.; Kortz, U. Selective Crystallization of Dimeric *vs.* Monomeric Dimethyltin-Containing Tungstoarsenates(III) and -antimonates(III) with the Guanidinium Cation. *Eur. J. Inorg. Chem*. **2009**, 947–953.
28. Piedra-Garza, L.F.; Reinoso, S.; Dickman, M.H.; Sanguineti, M.M.; Kortz, U. The First 3-Dimensional Assemblies of Organotin-Functionalized Polyanions. *Dalton Trans*. **2009**, 6231–6234.
29. Reinoso, S.; Bassil, B.S.; Barsukova, M.; Kortz, U. pH-Controlled Assemblies of Dimethyltin-Functionalized 9-Tungstophosphates with Guanidinium as Structure-Directing Cation. *Eur. J. Inorg. Chem*. **2010**, 2537–2542.
30. Iturrospe, A.; Artetxe, B.; Reinoso, S.; San Felices, L.; Vitoria, P.; Lezama, L.; Gutiérrez-Zorrilla, J.M. Copper(II) Complexes of Tetradentate Pyridyl Ligands Supported on Keggin Polyoxometalates: Single-Crystal to Single-Crystal Transformations Promoted by Reversible Dehydration Processes. *Inorg. Chem*. **2013**, *52*, 3084–3093.
31. Iturrospe, A.; San Felices, L.; Reinoso, S.; Artetxe, B.; Lezama, L.; Gutiérrez-Zorrilla, J.M. Reversible Dehydration in Polyoxometalate-Based Hybrid Compounds: A Study of Single-Crystal to Single-Crystal Transformations in Keggin-Type Germanotungstates Decorated with Copper(II) Complexes of Tetradentate N-Donor Ligands. *Cryst. Growth Des.* **2014**, *14*, 2318–2328.
32. Wéry, A.S.J.; Gutiérrez-Zorrilla, J.M.; Luque, A.; Ugalde, M.; Román, P. Phase Transitions in Metavanadates. Polymerization of Tetrakis(tert-Butylammonium)-cyclo-Tetrametavanadate *Chem. Mater.* **1996**, *8*, 408–413.
33. Ritchie, C.; Streb, C.; Thiel, J.; Mitchell, S.G.; Miras, H.N.; Long, D.-L.; Boyd, T.; Peacock, R.D.; McGlone, T.; Cronin, L. Reversible Redox Reactions in an Extended Polyoxometalate Framework Solid. *Angew. Chem.* **2008**, *47*, 6881–6884.
34. Thiel, J.; Ritchie, C.; Streb, C.; Long, D.-L.; Cronin, L. Heteroatom-Controlled Kinetics of Switchable Polyoxometalate Frameworks. *J. Am. Chem. Soc*. **2009**, *131*, 4180–4181.
35. Uehara, K.; Mizuno, N. Heterolytic Dissociation of Water Demonstrated by Crystal-to-Crystal Core Interconversion from (μ-Oxo)divanadium to Bis(μ-hydroxo)divanadium Substituted Polyoxometalates. *J. Am. Chem. Soc*. **2011**, *133*, 1622–1625.
36. Shi, L.-X.; Zhao, W.-F.; Xu, X.; Tang, J.; Wu, C.D. From 1D to 3D Single-Crystal-to-Single-Crystal Structural Transformations Based on Linear Polyanion $[Mn_4(H_2O)_{18}WZnMn_2(H_2O)_2(ZnW_9O_{34})_2]^{4-}$. *Inorg. Chem*. **2011**, *50*, 12387–12389.
37. Uchida, S.; Takahashi, E.; Mizuno, N. Porous Ionic Crystals Modified by Post-Synthesis of $K_2[Cr_3O(OOCH)_6(etpy)_3]_2[\alpha\text{-}SiW_{12}O_{40}]\cdot 8H_2O$ through Single-Crystal-to-Single-Crystal Transformation. *Inorg. Chem*. **2013**, *52*, 9320–9326.
38. Zhang, L.-Z.; Gu, W.; Liu, X.; Dong, Z.; Li, B. Solid-State Photopolymerization of a Photochromic Hybrid Based on Keggin Tungstophosphates. *CrystEngComm* **2008**, *10*, 652–654.
39. Zhang, L.-Z.; Gu, W.; Dong, Z.; Liu, X.; Li, B. Phase Transformation of a Rare-Earth Anderson Polyoxometalate at Low Temperature. *CrystEngComm* **2008**, *10*, 1318–1320.

40. Reinoso, S.; Dickman, M.H.; Praetorius, A.; Kortz, U. Low-Temperature Phase of Hexaguanidinium Heptamolybdate Monohydrate. *Acta Crystallogr*. **2008**, *E64*, m614–m615.
41. Barats-Damatov, D.; Shimon, L.J.W.; Feldman, Y.; Bendikov, T.; Neumann, R. Solid-State Crystal-to-Crystal Phase Transitions and Reversible Structure-Temperature Behavior of Phosphovanadomolybdic Acid, $H_5PV_2Mo_{10}O_{40}$. *Inorg. Chem*. **2015**, *4*, 628–634.
42. Chen, C.L.; Goforth, A.M.; Smith, M.D.; Su, C.Y.; zur Loye, H.-C. $[Co_2(ppca)_2(H_2O)(V_4O_{12})_{0.5}]$: A Framework Material Exhibiting Reversible Shrinkage and Expansion through a Single-Crystal-to-Single-Crystal Transformation Involving a Change in the Cobalt Coordination Environment. *Angew. Chem.* **2005**, *44*, 6673–6677.
43. Vittal, J.J. Supramolecular Structural Transformations Involving Coordination Polymers in the Solid State. *Coord. Chem. Rev*. **2007**, *251*, 1781–1795.
44. Abeysinghe, D.; Smith, M.D.; Yeon, J.; Morrison, G.; zur Loye, H.-C. Observation of Multiple Crystal-to-Crystal Transitions in a New Reduced Vanadium Oxalate Hybrid Material, $Ba_3[(VO)_2(C_2O_4)_5(H_2O)_6]\cdot(H_2O)_3$, Prepared via a Mild, Two-Step Hydrothermal Method. *Cryst. Growth Des*. **2014**, *14*, 4749–4758.
45. Tian, Y.; Allan, P.K.; Renouf, C.L.; He, X.; McCormick, L.J.; Morris, R.E. Synthesis and Structural Characterization of a Single-Crystal to Single-Crystal Transformable Coordination Polymer. *Dalton Trans*. **2014**, *43*, 1519–1523.
46. Hashemi, L.; Morsali, A.; Marandi, F.; Pantenburg, I.; Tehrani, A.A. Dynamic Crystal-to-Crystal Transformation of 1D to 2D Lead(II) Coordination Polymers by De- and Rehydration with No Change in the Morphology of Nano-Particles. *New J. Chem*. **2014**, *38*, 3375–3378.
47. Hanson, K.; Calin, N.; Bugaris, D.; Scancella, M.; Sevov, S.C. Reversible Repositioning of Zinc Atoms within Single Crystals of a Zinc Polycarboxylate with an Open-Framework Structure. *J. Am. Chem. Soc*. **2004**, *126*, 10502–10503.
48. Kitagawa, S.; Uemura, K. Dynamic Porous Properties of Coordination Polymers Inspired by Hydrogen Bonds. *Chem. Soc. Rev*. **2005**, *34*, 109–119.
49. Kitagawa, S.; Matsuda, R. Chemistry of Coordination Space of Porous Coordination Polymers. *Coord. Chem. Rev*. **2007**, *251*, 2490–2509.
50. Stamatatos, T.C.; Efthymiou, C.G.; Stoumpos, C.C.; Perlepes, S.P. Adventures in the Coordination Chemistry of Di-2-pyridyl Ketone and Related Ligands: From High-Spin Molecules and Single-Molecule Magnets to Coordination Polymers, and from Structural Aesthetics to an Exciting New Reactivity Chemistry of Coordinated Ligands. *Eur. J. Inorg. Chem*. **2009**, 3361–3368.
51. Huang, D.; Wang, W.; Zhang, X.; Chen, C.; Chen, F.; Liu, Q.; Liao, D.; Li, L.; Sun, L. Synthesis, Structural Characterizations and Magnetic Properties of a Series of Mono-, Di- and Polynuclear Manganese Pyridinecarboxylate Compounds. *Eur. J. Inorg. Chem.* **2004**, 1454–1464.
52. Biswas, C.; Mukherjee, P.; Drew, M.G.B.; Gómez-García, C.J.; Clemente-Juan, J.M.; Ghosh, A. Anion-Directed Synthesis of Metal-Organic Frameworks Based on 2-Picolinate Cu(II) Complexes: A Ferromagnetic Alternating Chain and Two Unprecedented Ferromagnetic Fish Backbone Chains. *Inorg. Chem.* **2007**, *46*, 10771–10780.
53. Pope, M.T.; Müller, A. Polyoxometalate Chemistry: An Old Field with New Dimensions in Several Disciplines. *Angew. Chem.* **1991**, *30*, 34–48.

54. Hervé, G.; Tézé, A.; Contant, R. General Principles of the Synthesis of Polyoxometalates in Aqueous Solution. In *Polyoxometalate Molecular Science*; Borrás-Almenar, J.J., Coronado, E., Müller, A., Pope, M.T., Eds.; Kluwer: Dordrecht, The Netherlands, 2003; NATO Science Series II. Volume 98, pp. 33–54.
55. Zhang, C.-J.; Pang, H.-J.; Tang, Q.; Chen, Y.-G. A Feasible Route to Approach 3D POM-Based Hybrids: Utilizing Substituted or Reduced Keggin Anions with High Charge Density. *Dalton Trans*. **2012**, *41*, 9365–9372.
56. San Felices, L.; Vitoria, P.; Gutiérrez-Zorrilla, J.M.; Lezama, L.; Reinoso, S. Hybrid Inorganic-Metalorganic Compounds Containing Copper(II)-Monosubstituted Keggin Polyanions and Polymeric Copper(I) Complexes. *Inorg. Chem.* **2006**, *45*, 7748–7757.
57. Żurowska, B.; Mroziński, J.; Ciunik, Z. One-Dimensional Copper(II) Compound with a Double Out-of-Plane Carboxylato-Bridge—Another Polymorphic Form of Cu(pyridine-2-carboxylate)$_2$. *Polyhedron* **2007**, *26*, 1251–1258.
58. Żurowska, B.; Mroziński, J.; Ślepokura, K. Structure and Magnetic Properties of a Double Out-of-Plane Carboxylato-Bridged Cu(II) Compound with Pyridine-2-carboxylate. *Polyhedron* **2007**, *26*, 3379–3387.
59. Woodward, P.M.; Sleight, A.W.; Vogt, T.J. Structure Refinement of Triclinic Tungsten Trioxide. *Phys. Chem. Solids* **1995**, *56*, 1305–1315.
60. Schofield, P.F.; Knight, K.S.; Redfern, S.A.T.; Cressey, G. Distortion Characteristics Across the Structural Phase Transition in ($Cu_{1-x}Zn_x$)WO_4. *Acta Crystallogr.* **1997**, *B53*, 102–112.
61. Tézé, A.; Hervé, G.; Finke, R.G.; Lyon, D.K. α-, β-, and γ-Dodecatungstosilicic Acids: Isomers and Related Lacunary Compounds. *Inorg. Synth.* **1990**, *27*, 85–96.
62. Hervé, G.; Tézé, A. Study of α and β-Enneatungstosilicates and Germanates. *Inorg. Chem.* **1977**, *16*, 2115–2117.
63. *CrysAlisPro Software System*, version 171.36.24; Agilent Technologies UK Ltd.: Oxford, UK, 2012.
64. Dolomanov, O.V.; Bourhis, L.J.; Gildea, R.J.; Howard, J.A.K.; Puschmann, H. A Complete Structure Solution, Refinement and Analysis Program. *J. Appl. Crystallogr.* **2009**, *42*, 339–341.
65. Sheldrick, G.M. A Short History of SHELX. *Acta Crystallogr.* **2008**, *A64*, 112–122.
66. Spek, A.L. Structure Validation in Chemical Crystallography. *Acta Crystallogr.* **2009**, *D65*, 148–155.
67. Farrugia, L.J. *WinGX* Suite for Small-Molecule Single-Crystal Crystallography. *J. Appl. Crystallogr.* **1999**, *32*, 837–836.